International Tables for Crystallography (2006). Vol. C, Section 4.3.8.3, pp. 422–424.

The axial three-beam fringes will coincide with the lattice planes, and show atom positions as dark if $\chi(u_{\mathbf{g}}) = (2n - 1/2)\pi$ and $\eta_0(t) - \eta_{\mathbf{g}}(t) = -\pi/2$. This total phase shift of $-\pi$ between Ψ_0 and the scattered beams is the desirable imaging condition for phase contrast, giving rise to dark atom positions on a bright background. This requires

$$C_s = (4n - 1)/(\lambda^3 u_{\mathbf{g}}^4) - 2\Delta f/(\lambda^2 u_{\mathbf{g}}^2)$$

as a condition for identical axial three-beam lattice images for $n = 0, 1, 2, \ldots$. This family of lines has been plotted in Fig. 4.3.8.3 for the (111) planes of silicon. Dashed lines denote the locus of 'white-atom' images (reversed contrast fringes), while the dotted lines indicate half-period images. In practice, the depth of field is limited by the finite illumination aperture θ_c, and few-beam lattice-image contrast will be a maximum at the stationary-phase focus setting, given by

$$\Delta f_0 = -C_s \lambda^2 u_{\mathbf{g}}^2. \quad (4.3.8.11)$$

This choice of focus ensures $\nabla\chi(u) = 0$ for $u = u_{\mathbf{g}}$, and thus ensures the most favourable trade-off between increasing θ_c and loss of fringe contrast for lattice planes **g**. Note that Δf_0 is not equal to the Scherzer focus Δf_s (see below). This focus setting is also indicated on Fig. 4.3.8.3, and indicates the instrumental conditions which produce the most intense (111) three- (or five-) beam axial fringes in silicon. For three-beam axial fringes of spacing d, it can be shown that the depth of field Δz is approximately

$$\Delta z = (\ln 2)^{1/2} d/\theta_c \pi. \quad (4.3.8.12)$$

This depth of field, within which strong fringes will be seen, is indicated as a boundary on Fig. 4.3.8.3. Thus, the finer the image detail, the smaller is the focal range over which it may be observed, for a given illumination aperture θ_c.

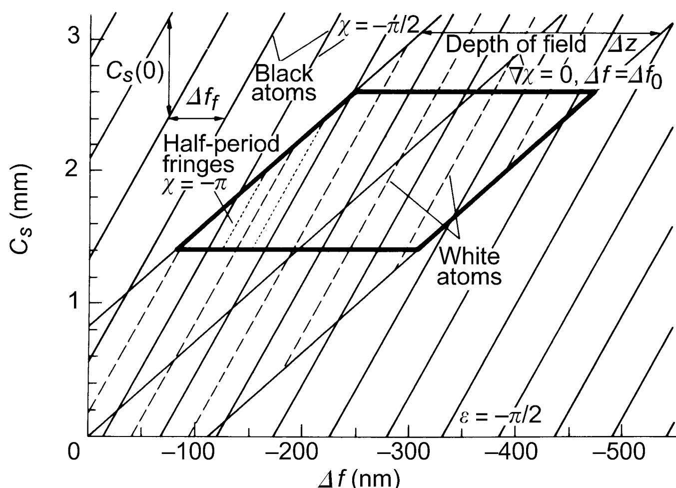

Fig. 4.3.8.3. A summary of three- (or five-) beam axial imaging conditions. Here, Δf_f is the Fourier image period, Δf_0 the stationary-phase focus, $C_s(0)$ the image period in C_s, and a scattering phase of $-\pi/2$ is assumed. The lines are drawn for the (111) planes of silicon at 100 kV with $\theta_c = 1.4$ mrad.

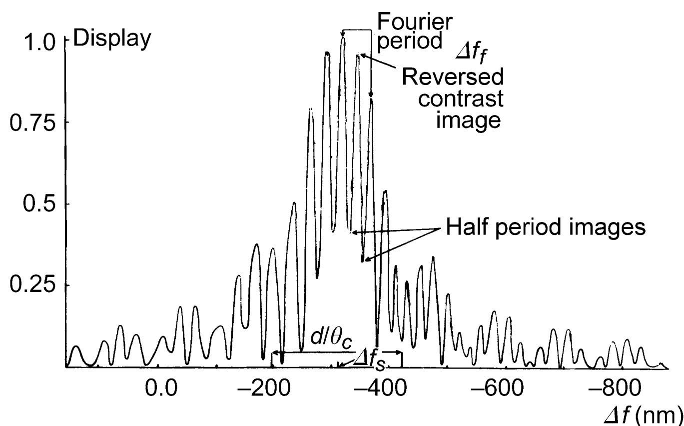

Fig. 4.3.8.4. The contrast of few-beam lattice images as a function of focus in the neighbourhood of the stationary-phase focus [see Olsen & Spence (1981)].

Fig. 4.3.8.4 shows an exact dynamical calculation for the contrast of three-beam axial fringes as a function of Δf in the neighbourhood of Δf_0. Both reversed contrast and half-period fringes are noted. The effects of electronic instabilities on lattice images are discussed in Subsection 4.3.8.3. It is assumed above that θ_c is sufficiently small to allow the neglect of any changes in diffraction conditions (Ewald-sphere orientation) within Θ_c. Under a similar approximation but without the approximations of transfer theory, Desseaux, Renault & Bourret (1977) have analysed the effect of beam divergence on two-dimensional five-beam axial lattice fringes.

When two-dimensional patterns of fringes are considered, the Fourier imaging conditions become more complex (see Subsection 4.3.8.3), but half-period fringe systems and reversed-contrast images are still seen. For example, in a cubic projection, a focus change of $\Delta f_f/2$ results in an image shifted by half a unit cell along the cell diagonal. It is readily shown that

$$\exp[i\chi(\Delta f)] = \exp[i\chi(\Delta f + \Delta f_f)]$$

if $\Delta f_f = 2na^2/\lambda + 2mb^2/\lambda$ when n, m are integers and a and b are the two dimensions of any orthogonal unit cell that can be chosen for $\Psi_p(x, y)$. Thus, changes in focus by $\Delta f_f(n, m)$ produce identical images in crystals for which such a cell can be chosen, regardless of the number of beams contributing (Cowley & Moodie, 1960).

For closed-form expressions for the few-beam (up to 10 beams) two-dimensional dynamical Bragg-beam amplitudes $\Psi_{\mathbf{g}}$ in orientations of high symmetry, the reader is referred to the work of Fukuhara (1966).

4.3.8.3. *Crystal structure images*

We define a crystal structure image as a high-resolution electron micrograph that faithfully represents a projection of a crystal structure to some limited resolution, and which was obtained using instrumental conditions that are independent of the structure, and so require no *a priori* knowledge of the structure. The resolution of these images is discussed in Subsection 4.3.8.6, and their variation with instrumental parameters in Subsection 4.3.8.4.

Equation (4.3.8.2) must now be modified to take account of the finite electron source size used and of the effects of the range of energies present in the electron beam. For a perfect crystal we may write, as in equation (2.5.1.36) in *IT* B (1992),

$$I_T(\mathbf{r}) = \iint |\psi(\mathbf{u}', \Delta f, \mathbf{r})|^2 G(\mathbf{u}') B(\Delta f, \mathbf{u}') \,\mathrm{d}\mathbf{u}' \,\mathrm{d}\Delta f \quad (4.3.8.13a)$$

for the total image intensity due to an electron source whose normalized distribution of wavevectors is $G(\mathbf{u}')$, where $\mathbf{u}'$ has components u_1, v_1, and which extends over a range of energies corresponding to the distribution of focus $B(\Delta f, \mathbf{u})$. If χ is also assumed to vary linearly across θ_c and changes in the diffraction conditions over this range are assumed to make only negligible changes in the diffracted-beam amplitude $\Psi_{\mathbf{g}}$, the expression for a Fourier coefficient of the total image intensity $I_T(\mathbf{r})$ becomes

Copyright © 2006 International Union of Crystallography

$$I_{\mathbf{g}} = \sum_{\mathbf{h}} \Psi_{\mathbf{h}} \exp\{-i\chi(\mathbf{h})\}\gamma\{\nabla\chi(\mathbf{h}) - \nabla\chi(\mathbf{h}-\mathbf{g})\} \times \psi^*_{\mathbf{h}-\mathbf{g}} \exp\{i\chi(\mathbf{h}-\mathbf{g})\}\beta\{\tfrac{1}{2}(\mathbf{h}^2 - |\mathbf{h}-\mathbf{g}|^2)^2\}, \quad (4.3.8.13b)$$

where $\gamma(\mathbf{h})$ and $\beta(\mathbf{g})$ are the Fourier transforms of $G(\mathbf{u}')$ and $B(\Delta f, \mathbf{u}')$, respectively.

For the imaging of very thin crystals, and particularly for the case of defects in crystals, which are frequently the objects of particular interest, we give here some useful approximations for HREM structure images in terms of the continuous projected crystal potential

$$\varphi(x, y) = (1/t)\int_0^t \varphi(x, y, z)\,\mathrm{d}z,$$

where the projection is taken in the electron-beam direction. A brief summary of the use of these approximations is included in Section 2.5.1 of *IT* B (1992) and computing methods are discussed in Subsection 4.3.8.5 and Section 4.3.4.

The projected-charge-density (PCD) approximation (Cowley & Moodie, 1960) gives the HREM image intensity (for the simplified case where $C_s = 0$) as

$$I(x, y) = 1 + (\Delta f \lambda\sigma/2\pi\varepsilon_0\varepsilon)\rho_p(x, y), \quad (4.3.8.13c)$$

where $\rho_p(x, y)$ is the projected charge density for the specimen (including the nuclear contribution) and is related to $\varphi_p(x, y)$ through Poisson's equation. Here, $\varepsilon_0\varepsilon$ is the specimen dielectric constant. This approximation, unlike the weak-phase-object approximation (WPO), includes multiple scattering to all orders of the Born series, within the approximation that the component of the scattering vector is zero in the beam direction (a 'flat' Ewald sphere). Contrast is found to be proportional to defocus and to $\rho_p(x, y)$. The failure conditions of this approximation are discussed by Lynch, Moodie & O'Keefe (1975); briefly, it fails for $\chi(u_0) > \pi/2$ (and hence if C_s, Δf or u_0 becomes large) or for large thicknesses t ($t < 7$ nm is suggested for specimens of medium atomic weight and $\lambda = 0.037$ Å). The PCD result becomes increasingly accurate with increasing accelerating voltage for small C_s.

The WPO approximation has been used extensively in combination with the Scherzer-focus condition (Scherzer, 1949) for the interpretation of structure images (Cowley & Iijima, 1972). This approximation neglects multiple scattering of the beam electron and thereby allows the application of the methods of linear transfer theory from optics. The image intensity is then given, for plane-wave illumination, by

$$\begin{aligned} I(x, y) &= 1 + 2\sigma\varphi_p(x, y) * \mathcal{F}\{\sin\chi(u, v)P(u, v)\} \\ &= 1 + 2\sigma\varphi_p(x, y) * S(x, y), \end{aligned} \quad (4.3.8.14)$$

where $\mathcal{F}$ denotes Fourier transform, $*$ denotes convolution, and u and v are orthogonal components of the two-dimensional scattering vector $\mathbf{u}$. The function $S(x, y)$ is sharply peaked and negative at the 'Scherzer focus'

$$\Delta f = \Delta f_s = 1.2(C_s\lambda)^{1/2} \quad (4.3.8.15a)$$

and the optimum objective aperture size

$$\theta_0 = 1.5(\lambda/C_s)^{1/4}. \quad (4.3.8.15b)$$

It forms the impulse response of an electron microscope for phase contrast. Contrast is found to be proportional to φ_p and to the interaction parameter σ, which increases very slowly with accelerating voltage above about 500 keV. The point resolution [see Subsection 2.5.1.9 of *IT* B (1992) and Subsection 4.3.8.6] is conventionally defined from equation (4.3.8.15*b*) as λ/θ_0, or

$$d_p = 0.66\, C_s^{1/4}\lambda^{3/4}. \quad (4.3.8.16)$$

The occurrence of appreciable multiple scattering, and therefore of the failure of the WPO approximation, depends on specimen thickness, orientation, and accelerating voltage. Detailed comparisons between accurate multiple-scattering calculations, the PCD approximation, and the WPO approximation can be found in Lynch, Moodie & O'Keefe (1975) and Jap & Glaeser (1978). As a very rough guide, equation (4.3.8.14) can be expected to fail for light elements at 100 keV and thicknesses greater than about 5.0 nm. Multiple-scattering effects have been predicted within single atoms of gold at 100 keV.

The WPO approximation may be extended to include the effects of an extended source (partial spatial coherence) and a range of incident electron-beam energies (temporal coherence). General methods for incorporating these effects in the presence of multiple scattering are described in Subsection 4.3.8.5. Under the approximations of linear imaging outlined below, it can be shown (Wade & Frank, 1977; Fejes, 1977) that $\sin\chi(u, v)P(u, v)$ in equation (4.3.8.14) may be replaced by

$$\begin{aligned} A'(\mathbf{u}) &= P(\mathbf{u})\exp[i\chi(\mathbf{u})]\exp(-\pi^2\Delta^2\lambda^2\mathbf{u}^4/2)\gamma(\nabla\chi/2\pi) \\ &= P(\mathbf{u})\exp[i\chi(\mathbf{u})]\exp(i\pi^2\Delta^2\lambda^2\mathbf{u}^4/2)\exp(-\pi^2u_0^2q) \end{aligned} \quad (4.3.8.17)$$

if astigmatism is absent. Here, $\mathbf{u} = u\mathbf{i} + v\mathbf{j}$ and $|\mathbf{u}| = 2\theta/\lambda = (u^2 + v^2)^{1/2}$. In addition, $\gamma(\mathbf{u}')$ is the Fourier transform of the source intensity distribution (assumed Gaussian), so that $\gamma(\nabla\chi/2\pi)$ is small in regions where the slope of $\chi(\mathbf{u}')$ is large, resulting in severe attenuation of these spatial frequencies. If the illuminating beam divergence Θ_c is chosen as the angular half width for which the distribution of source intensity falls to half its maximum value, then

$$\theta_c = \lambda u_0(\ln 2)^{1/2}. \quad (4.3.8.18)$$

The quantity q is defined by

$$q = (C_s\lambda^3\mathbf{u}^3 + \Delta f\lambda\mathbf{u})^2 + T2,$$

where $T2$ expresses a coupling between the effects of partial spatial coherence and temporal coherence. This term can frequently be neglected under HREM conditions [see Wade & Frank (1977) for details]. The damping envelope due to chromatic effects is described by the parameter

$$\Delta = C_cQ = C_c\{[\sigma^2(V_0)]/V_0^2 + [4\sigma^2(I_0)]/I_0^2 + [\sigma^2(E_0)]/E_0^2\}^{1/2}, \quad (4.3.8.19)$$

where $\sigma^2(V_0)$ and $\sigma^2(I_0)$ are the variances in the statistically independent fluctuations of accelerating voltage V_0 and objective-lens current I_0. The r.m.s. value of the high voltage fluctuation is equal to the standard deviation $\sigma(V_0) = [\sigma^2(V_0)]^{1/2}$. The full width at half-maximum height of the energy distribution of electrons leaving the filament is

$$\Delta E = 2(2\ln 2)^{1/2}\sigma(E_0) = 2.355[\sigma^2(E_0)]^{1/2}. \quad (4.3.8.20)$$

Here, C_c is the chromatic aberration constant of the objective lens.

Equations (4.3.8.14) and (4.3.8.17) indicate that under linear imaging conditions the transfer function for HREM contains a chromatic damping envelope more severely attenuating than a Gaussian of width

$$U_0(\Delta) = [2/\pi\lambda\Delta]^{1/2},$$

which is present in the absence of any objective aperture $P(\mathbf{u})$. The resulting resolution limit

$$d_i = [\pi\lambda\Delta/2]^{1/2} \qquad (4.3.8.21)$$

is known as the information resolution limit (see Subsection 4.3.8.6) and depends on electronic instabilities and the thermal-energy spread of electrons leaving the filament. The reduction in the contribution of particular diffracted beams to the image due to limited spatial coherence is minimized over those extended regions for which $\nabla\chi(\mathbf{u})$ is small, called passbands, which occur when

$$\Delta f_n = [C_s\lambda(8n+3)/2]^{1/2}. \qquad (4.3.8.22)$$

The Scherzer focus Δf_s corresponds to $n = 0$. These passbands become narrower and move to higher $\mathbf{u}$ values with increasing n, but are subject also to chromatic damping effects. The passbands occur between spatial frequencies U_1 and U_2, where

$$U_{1,2} = C_s^{-1/4}\lambda^{-3/4}\{[(8n+2)/2]^{1/2} \pm 1\}^{1/2}. \qquad (4.3.8.23)$$

Their use for extracting information beyond the point resolution of an electron microscope is further discussed in Subsection 4.3.8.6.

Fig. 4.3.8.5 shows transfer functions for a modern instrument for $n = 0$ and 1. Equations (4.3.8.14) and (4.3.8.17) provide a simple, useful, and popular approach to the interpretation of HREM images and valuable insights into resolution-limiting factors. However, it must be emphasized that these results apply only (amongst other conditions) for $\Phi_0 \gg \Phi_{\mathbf{g}}$ (in crystals) and therefore do not apply to the usual case of strong multiple electron scattering. Equation (4.3.8.13*b*) does not make this approximation. In real space, for crystals, the alignment of columns of atoms in the beam direction rapidly leads to phase changes in the electron wavefunction that exceed $\pi/2$, leading to the failure of equation (4.3.8.14). Accurate quantitative comparisons of experimental and simulated HREM images must be based on equation (4.3.8.13*a*), or possibly (4.3.8.13*b*), with $\psi(\mathbf{u}', \Delta f, \mathbf{r})$ obtained from many-beam dynamical calculations of the type described in Subsection 4.3.8.5.

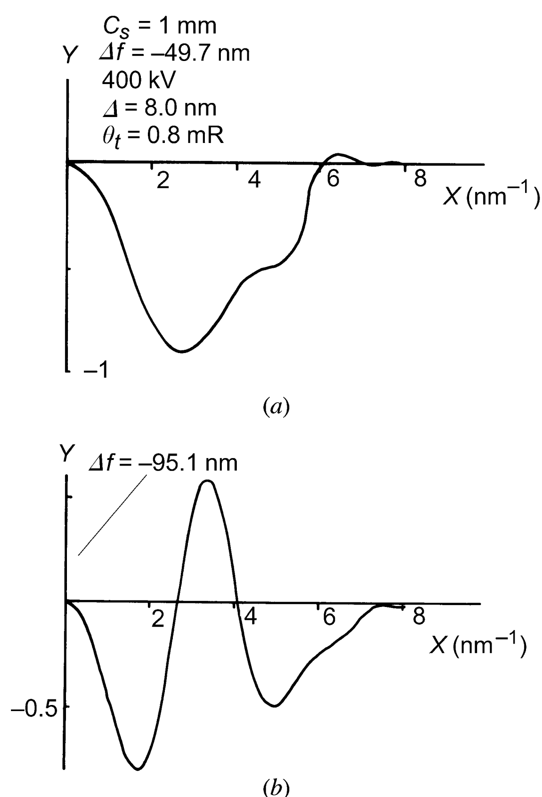

Fig. 4.3.8.5. (*a*) The transfer function for a 400 kV electron microscope with a point resolution of 1.7 Å at the Scherzer focus; the curve is based on equation (4.3.8.17). In (*b*) is shown a transfer function for similar conditions at the first 'passband' focus [$n = 1$ in equation (4.3.8.22)].

For the structure imaging of specific types of defects and materials, the following references are relevant. (i) For line defects viewed parallel to the line, d'Anterroches & Bourret (1984); viewed normal to the line, Alexander, Spence, Shindo, Gottschalk & Long (1986). (ii) For problems of variable lattice spacing (*e.g.* spinodal decomposition), Cockayne & Gronsky (1981). (iii) For point defects and their ordering, in tunnel structures, Yagi & Cowley (1978); in semiconductors, Zakharov, Pasemann & Rozhanski (1982); in metals, Fields & Cowley (1978). (iv) For interfaces, see the proceedings reported in *Ultramicroscopy* (1992), Vol. 40, No. 3. (v) For metals, Lovey, Coene, Van Dyck, Van Tendeloo, Van Landuyt & Amelinckx (1984). (vi) For organic crystals, Kobayashi, Fujiyoshi & Uyeda (1982). (vii) For a general review of applications in solid-state chemistry, see the collection of papers reported in *Ultramicroscopy* (1985), Vol. 18, Nos. 1–4. (viii) Radiation-damage effects are observed at atomic resolution by Horiuchi (1982).

4.3.8.4. *Parameters affecting HREM images*

The *instrumental parameters* that affect HREM images include accelerating voltage, astigmatism, optic-axis alignment, focus setting Δf, spherical-aberration constant C_s, beam divergence θ_c, and chromatic aberration constant C_c. Crystal parameters influencing HREM images include thickness, absorption, ionicity, and the alignment of the crystal zone axis with the beam, in addition to the structure factors and atom positions of the sample. The accurate measurement of electron wavelength or accelerating voltage has been discussed by many workers, including Uyeda, Hoier and others [see Fitzgerald & Johnson (1984) for references]. The measurement of Kikuchi-line spacings from crystals of known structure appears to be the most accurate and convenient method for HREM work, and allows an overall accuracy of better than 0.2% in accelerating voltage. Fluctuations in accelerating voltage contribute to the chromatic damping term Δ in equation (4.3.8.19) through the variance $\sigma^2(V_0)$. With the trend toward the use of higher accelerating voltages for HREM work, this term has become especially significant for the consideration of the information resolution limit [equation (4.3.8.21)].

Techniques for the accurate measurement of astigmatism and chromatic aberration are described by Spence (1988). The displacement of images of small crystals with beam tilt may be used to measure C_s; alternatively, the curvature of higher-order Laue-zone lines in CBED patterns has been used. The method of Budinger & Glaeser (1976) uses a similar dark-field image-displacement method to provide values for both Δf and C_s, and appears to be the most convenient and accurate for HREM work. The analysis of optical diffractograms initiated by Thon and co-workers from HREM images of thin amorphous films provides an invaluable diagnostic aid for HREM work; however, the determination of C_s by this method is prone to large errors, especially at small defocus. Diffractograms provide a rapid method for the determination of focus setting (see Krivanek, 1976) and in addition provide a sensitive indicator of specimen movement, astigmatism, and the damping-envelope constants Δ and Θ_c.

references